Petroleum Science 23 (2026) 2485–2500

Contents lists available at ScienceDirect

Petroleum Science

journal homepage: www.keaipublishing.com/en/journals/petroleum-science

Original Paper

The present-day stress state and its impact on drilling and reservoir management in a field of the Abadan Plain, Southwest Iran

Mohsen Ezati [a], Ali Kadkhodaie [a,*], Vahid Bolandi [b]

[a] Earth Sciences Department, Faculty of Natural Sciences, University of Tabriz, Tabriz, 5166616471, Iran
[b] Pezhvak Energy–PECO, Tehran, 1469644307, Iran

ARTICLE INFO

Article history:
Received 21 February 2025
Received in revised form
29 November 2025
Accepted 23 January 2026
Available online 30 January 2026

Edited by Meng-Jiao Zhou

Keywords:
Geomechanical modeling
Stress state
Borehole breakouts
Induced fractures
Abadan plain

ABSTRACT

The present-day stress state of the Abadan Plain in Southwest Iran is a critical factor in the management of drilling operations and reservoir development. This research integrates multiple data sources, including borehole image logs, leak-off test (LOT) data and petrophysical logs from 11 wells, to characterize the regional stress field. Borehole breakouts and drilling induced fractures were analyzed to identify the orientation of the maximum horizontal stress (S_{Hmax}), which was found to consistently align in a northeast-southwest direction across the region. Using a stress polygon method, results showed that the S_{Hmax} values ranged from 50.78 MPa to 62.1 MPa in the Gurpi Formation, from 92.91 MPa to 116.82 MPa in the Gadvan Formation and between 114.48 MPa and 127.23 MPa in the Fahliyan Formation. The results also revealed that the region exhibits a consistent strike-slip stress regime, with S_{Hmax} > vertical stress (S_V) > minimum horizontal stress (S_{hmin}) in multiple wells, which has important implications for fault reactivation and drilling operations. These insights are crucial for improving drilling practices, understanding fault reactivation, and making informed decisions for future exploration and development in the area.

1. Introduction

The state of in-situ stress plays a crucial role in drilling and reservoir development. It governs wellbore stability, selection of bit type, planning of well trajectory, casing design, mud weight window determination, hydraulic fracturing efficiency, and the likelihood of fault reactivation (Ezati et al., 2014, 2020; Bondur et al., 2016; Radwan and Sen, 2021; Saadatnia et al., 2022, 2024; Kumar et al., 2023; Rajabi et al., 2024). Successful characterization of the stress regime is therefore a prerequisite for safe and efficient field operations.

The Abadan Plain is a structurally complex region dominated by both Arabian-type basement-cored anticlines and the Zagros Fold–Thrust Belt. Abdollahie Fard et al. (2006) illustrated that gentle N–S to NE–SW trending anticlines are accompanied by NW–SE thrust-related folds, reflecting the interaction between deep-seated basement faults and salt tectonics. This highlights the dual control of basement involvement and salt migration on structural evolution. Rajabi et al. (2010) further showed, using Ilam Formation image logs, that one fracture set is parallel to the present-day maximum horizontal stress (S_{Hmax}), and other fracture systems preserve older tectonic records of the Zagros orogeny. These findings attest to the correlation between inherited structures and recent stress indicators in the region.

Other studies have contributed to characterizing both stress orientation and magnitude. Ezati et al. (2019) linked Sarvak Formation micro-fractures to porosity–permeability anomalies and noted their localized effect and limited contribution to regional reservoir quality. Reisabadi et al. (2018) constructed a one-dimensional mechanical earth model (1-D MEM) for the Abadan Plain and identified a consistent NE–SW S_{Hmax} orientation from borehole breakouts. Similarly, Yaghoubi et al. (2021) analyzed wells and focal mechanism data in the Dezful Embayment and supported a compressional state of stress in the basement and a normal/strike-slip regime in the sedimentary cover. The conclusions are also similar to show a NE–SW orientation of S_{Hmax} in the Abadan Plain. These studies together support a broadly uniform orientation of stresses but have concerns about uncertainties in magnitudes of stress and their changes over formations.

* Corresponding author.
E-mail address: kadkhodaie_ali@tabrizu.ac.ir (A. Kadkhodaie).
Peer review under the responsibility of China University of Petroleum (Beijing).

https://doi.org/10.1016/j.petsci.2026.01.041

Nomenclature:

ε_x	Tectonic strain on *x* plane
ε_y	Tectonic strain on *y* plane
BS	Bit size
c	Cohesion
CV	Coefficient of variation
DIF	Drilling induced fracture
DT	Slowness of compressional wave
DT_{NCT}	Normal compaction trend
E	Young's modulus
FMI	Fullbore formation microimager
GR	Gamma ray
LOP	Leak-off point
LOT	Leak-off test
MDT	Modular formation dynamics tester
MEM	Mechanical earth model
n	Eaton's exponent
Phyd	Hydrostatic pore pressure
P_P	Pore pressure
S_{Hmax}	Maximum horizontal stress
S_{hmin}	Minimum horizontal stress
STAR	Simultaneous acoustic and resistivity
S_V	Vertical stress
UBI	Ultrasonic borehole imaging
UCS	Unconfined compressive strength
UGC Map	Underground contour map
WSM	World stress map
XLOT	Extended leak-off test
XRMI	X-tended range micro imaging
ν	Poisson's ratio
σ_1	Maximum principal stress
σ_3	Minimum principal stress
σ_θ	Tangential stress
ϕ	Friction angle
α	Biot's coefficient
μ	Friction coefficient

At a broader scale, the World Stress Map (Heidbach et al., 2016) indicates a dominant NE–SW S_{Hmax} direction in the study area, which is consistent with local borehole breakout data (Fig. 1). Recent global advances also inform stress analysis in this region. For instance, Zhou et al. (2022, 2024) showed how elevated temperatures and stresses reduce rock strength, Cao et al. (2024) proposed improved fracture density corrections, and Fang et al. (2025) and Yanchun et al. (2024) provided sophisticated model methods for simulating reservoir performance. Dong et al. (2024) highlighted permeability enhancement by thermal effects, while Zhang et al. (2023) emphasized the impact of cyclic loading on stress sensitivity. These studies provide valuable methodological insights that are directly relevant for interpreting image logs and geomechanical behavior in the Abadan Plain.

This study presents an integrated approach to estimating horizontal stresses by integrating a variety of data sources, including leak-off test (LOT) data, borehole wall failure observations, and rock mechanics information. The key contributions of this research include the combination of borehole imaging logs, LOT data, pore pressure, and rock mechanical properties, which improve the accuracy of stress models and reduce uncertainties. The study also utilizes advanced modeling techniques for estimating horizontal stresses in the absence of LOT data, using alternative tools like induced fractures and borehole breakouts. Furthermore, the research provides insights into the stress state in the studied oilfield, particularly in formations with complex geological and geomechanical characteristics, marking an important advancement in stress state analysis in the region.

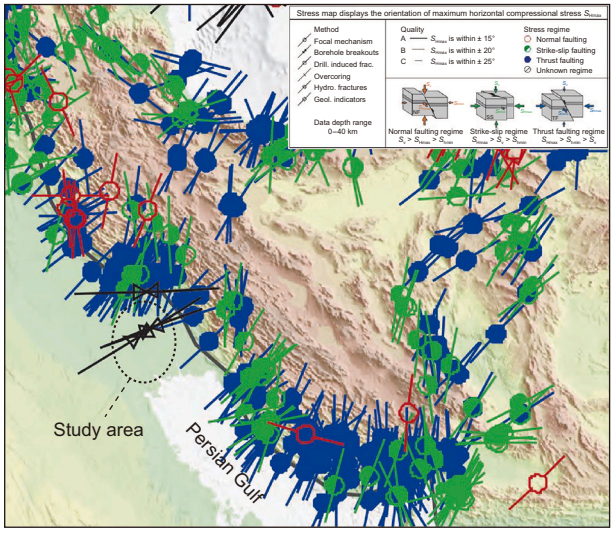

Fig. 1. The world stress map by Heidbach et al. (2016), highlighting the identified horizontal stress directions in the study area.

2. Geological setting

The studied oilfield is an N-S trending anticline located in Abadan Plain, southwest Iran. It is 80 km west of Ahvaz city (Fig. 2). Abadan Plain has three main structural trends: NE–SW, N–S and NW–SE which are related to deep-seated fault activities (Abdollahie Fard et al., 2006). Many of the structures associated with the mentioned trends in Abadan Plain are related to reactivation of basement-rooted normal faults which caused forced-folding in overlying sediments (Sattarzadeh et al., 2002).

Seismic data and wells in the studied field reveal erosional surfaces linked to the uplift of basement-cored horsts (Fig. 3), with channels observed at the top of the Sarvak Formation in 3-D seismic data. An E-W seismic section shows steep faults in the anticline core, stopping at the Upper Jurassic Gotnia Formation. Four production layers—Sarvak, Kazhdumi, Gadvan, and Fahliyan—are identified in the field. The southern part of the field features a large N-S trending anticline, part of the Arabian Trend, in contrast to the NW-SE trending fields in the Dezful Embayment (Abdollahie Fard et al., 2006).

The faults and folds of the Zagros region, near the Abadan Plain, are located within the Zagros foreland basins, which are elongate sedimentary troughs formed between a fold-and-thrust belt and an undeformed craton (Dickinson, 1974; Beaumont, 1981; Jordan, 1981; DeCelles and Giles, 1996). The Persian Gulf, Abadan Plain, and Mesopotamian are part of the foreland basin in the outermost Zagros orogenic belt (Edgell, 1996; Abdollahie Fard et al., 2006; Stewart, 2018). The Khurais-Burgan palaeo-high is an important structural feature in the western Abadan Plain, where the studied oilfield in Iran and the Burgan in Kuwait and Khurais-Burgan anticline in Saudi Arabia are located (Al-Husseini, 2000). Late

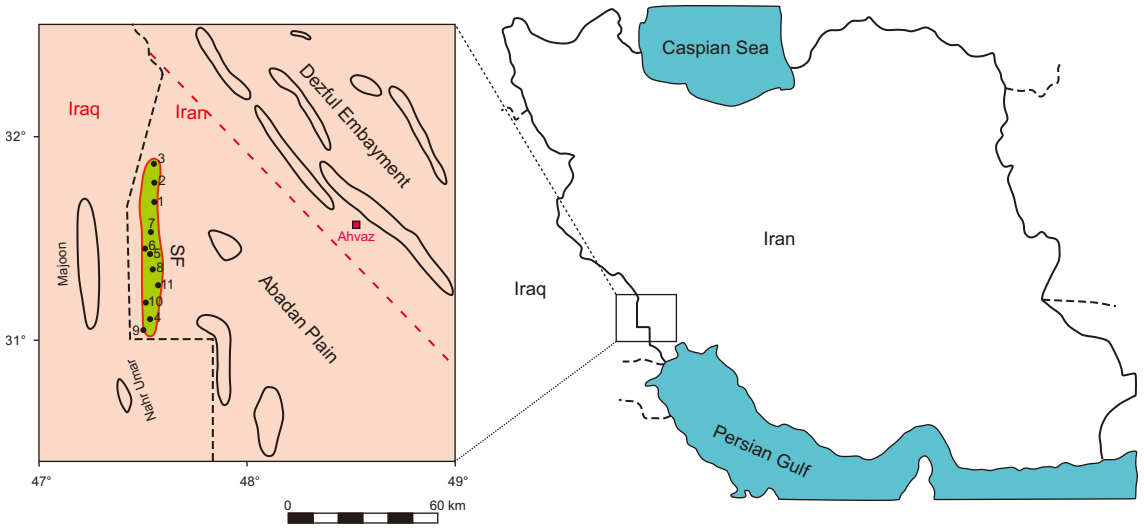

Fig. 2. The field location map, situated in the Abadan Plain, SW Iran.

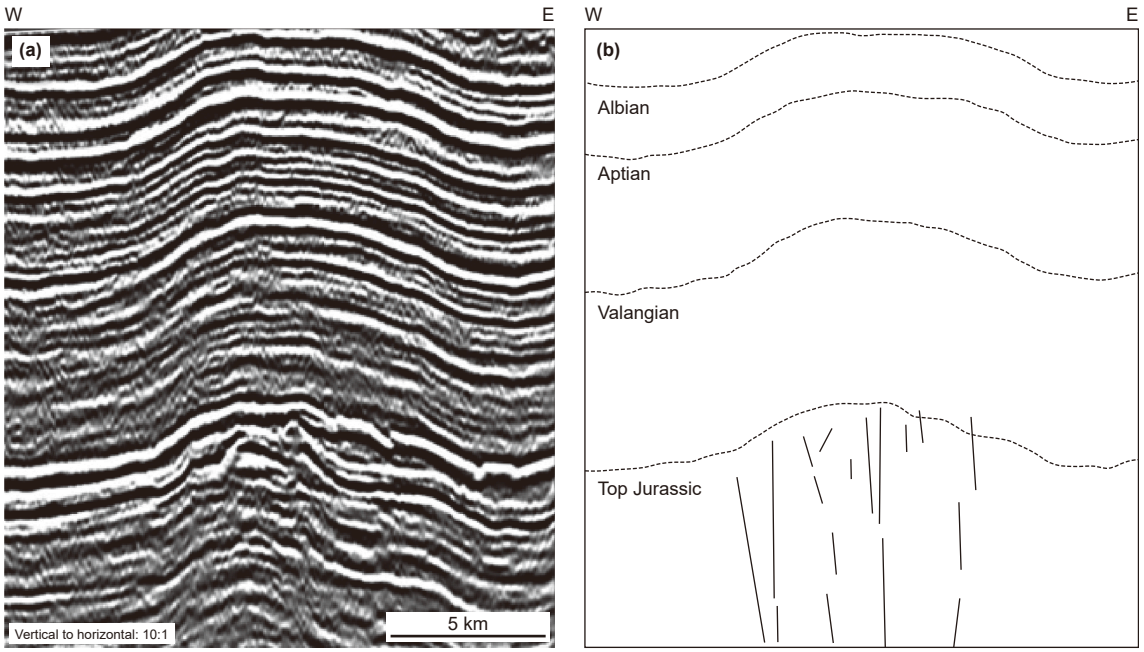

Fig. 3. A seismic section of the investigated oilfield shows multiple steep faults situated at the core of the anticline, which extend down to the Upper Jurassic layers (Abdollahie Fard et al., 2006).

Cretaceous and Oligo-Miocene sediments are thinner above the Khurais-Burgan palaeo-high due to syn-sedimentary reactivation of the inherited basement structure (Lalami et al., 2020).

The Abadan Plain Basin, located at the north-western corner of the Persian Gulf, is one of the most prolific hydrocarbon basins in the region and was among the first to produce oil commercially (Atashbari et al., 2018; Assadi et al., 2023). This basin is bounded by the Dezful Embayment to the north and east. The deepest well of the Abadan Plain area was drilled in the studied field (Fig. 4), reaching the top of the Neyriz Formation, making it a key well for the study area. The geological framework of the Abadan Plain resembles that of the Mesopotamian Basin, with similar stratigraphy and tectonic history (Assadi et al., 2023; Mehrabi et al., 2023; Abbasi et al., 2024).

Lithology and reservoir facies change significantly across the Khurais-Burgan high due to the interaction of sea level changes and tectonic activities. The Khurais-Burgan basement faulting system shows a deepening and thickening trend of the Basin toward the NE, with increasing sedimentation rate and formation thickness from the Mesopotamian Basin (SW) to the Dezful Embayment (NE) during deposition of the Gotnia-Gachsaran successions. Reactivation of the basement faults also resulted in facies changes across the Basin (Assadi et al., 2023).

Recent studies have further advanced our understanding of the tectonics and geological characteristics of the Abadan Plain region. Atashbari et al. (2018), provided a comprehensive review of the Abadan Plain Basin's tectonics, highlighting the influence of the Zagros Fold-Thrust-Belt on structural development and

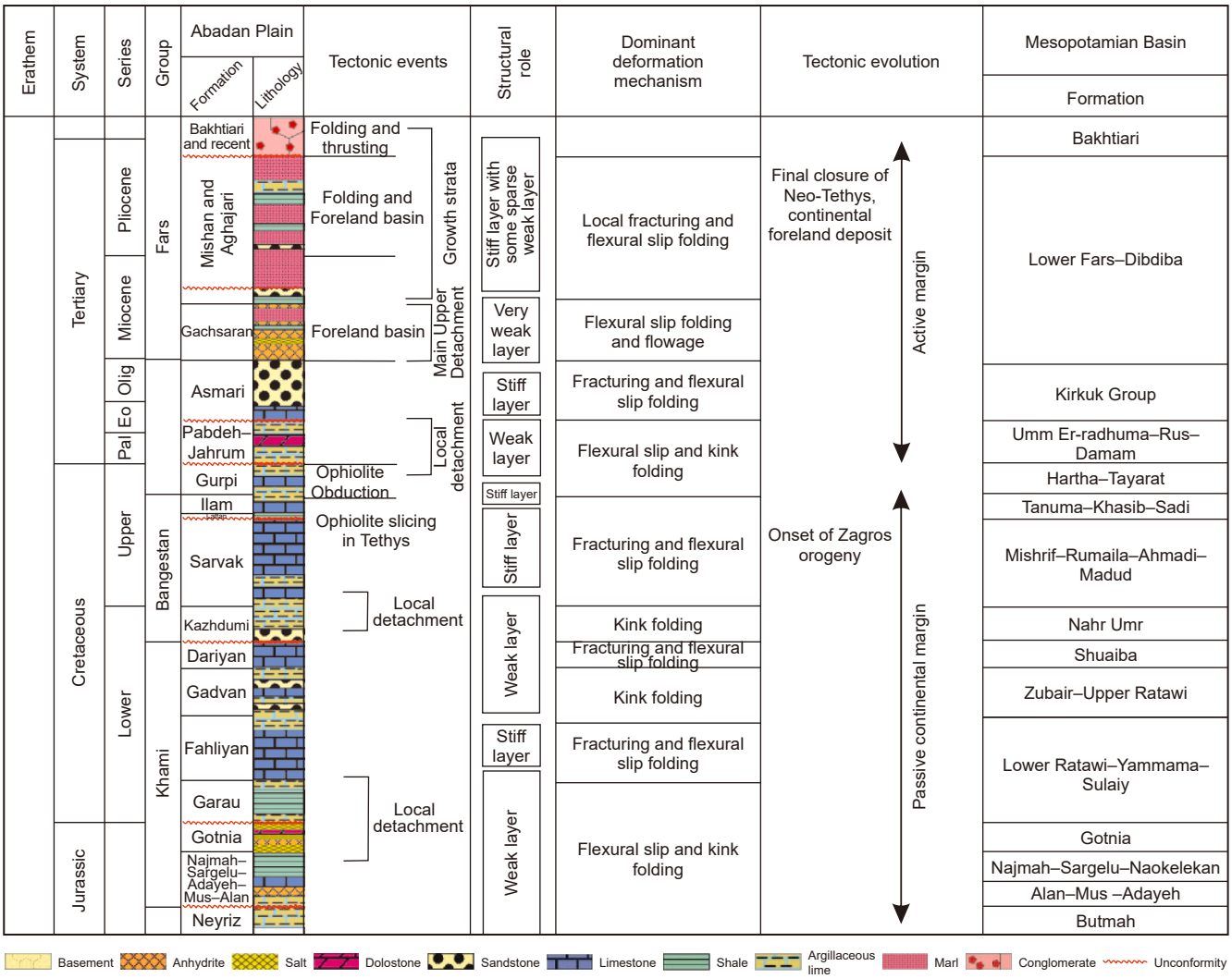

Fig. 4. The stratigraphy column of the study area. The column illustrates the dominant lithology from the Neyriz to Aghajari formations (modified after Shamszadeh et al., 2022).

hydrocarbon accumulation, emphasizing the role of basement-rooted fault reactivation. Tavoosi et al. (2023), investigated the petrophysical heterogeneity of the Fahliyan Formation, showing that diagenetic processes like dissolution and cementation control reservoir quality and affect the region's tectonic evolution. Abbasi et al. (2024), examined the diagenetic evolution of the Sarvak Formation, highlighting the role of tectonic activities and eustatic sea level fluctuations in shaping processes such as karstification and brecciation.

3. Methods and materials

3.1. Materials

This study used data from 11 wells to determine the in-situ stress state. The data included petrophysical logs (Density, Neutron, Sonic etc.), borehole image logs (borehole breakout and drilling induced fracture detection), modular formation dynamics tester (MDT), geological and geophysical data (seismic data, formation tops), and geomechanical data (Table 1). The geomechanical data was leak-off tests (LOT) to determine minimum principal stress magnitude, unconfined compressive strength (UCS) tests, tensile strength, Poisson's ratio and Young's modulus.

Table 1
List of the wells with the corresponding data.

Well name	Petrophysical logs	Image Log	MDT	LOT	Drilling report
Well-01	✓	✓			✓
Well-02	✓	✓			✓
Well-03	✓	✓			✓
Well-04	✓	✓	✓		✓
Well-05	✓	✓	✓		✓
Well-06	✓	✓	✓		✓
Well-07	✓	✓	✓		✓
Well-08	✓	✓			✓
Well-09	✓	✓	✓	✓	✓
Well-10	✓	✓	✓	✓	✓
Well-11	✓	✓			✓

All of which are required to characterize rock mechanical properties. This data was then integrated to build a model of the in-situ stress state.

To ensure the quality of the petrophysical data, their reading standards were evaluated across different lithologies. Additionally, their overlap and separation in key layers were assessed. The QC of image logs' inclinometry was also carried out in all wells to ensure the accuracy of the extracted features' orientations. Furthermore,

before interpreting the image logs, necessary corrections, including speed, bad button, and swing arm corrections, were applied. For the seismic data, its integrity is checked to identify any missing or corrupted information. Pre-processing techniques, such as noise filtering and signal correction, are applied to enhance data clarity. Regular calibration of equipment, including geophones and sensors, ensures accurate measurements. Additionally, seismic data are cross-validated with other datasets, such as well logs or geological models, to verify consistency.

All wells analyzed in this study are nearly vertical, with inclinations of less than 4°, which ensures reliable determination of horizontal stress orientations (Table 2). Both electrical (FMI/XRMI/STAR) and ultrasonic (UBI) image logs were utilized depending on data availability in each well. Electrical image logs provided high resolution resistivity contrasts for the accurate identification of breakouts, while ultrasonic logs allowed complete 360° coverage of the borehole wall, enabling detailed visualization of failure geometry, especially in Well-05. Combination of these two log types enhanced confidence in interpretation related to drilling-induced fractures and breakouts.

3.2. Methods

The pore pressure in the studied wells was calculated using two data sources. The baseline hydrostatic pressure was determined from the depth–pressure gradient (saline water equivalent). Deviations from this baseline in drilling reports and pressure–depth plots indicated zones of overpressure. Main data sources were MDT measurements and well-test data, all cross-checked against converted mud weights during drilling. The MDT measures pore pressure by isolating a small section of the formation with a rubber packer seal and withdrawing fluid from the formation through a probe. Once the packer seals against the borehole wall, pressure gauges within the tool record the build-up curve as formation fluid flows into the chamber of the tool. In static conditions, the pressure stabilizes at the formation's equilibrium pore pressure. The measurements are taken at multiple depths to detect pressure changes with depth, identify overpressure zones.

Overpressure evidence was observed in several formations, most prominently the Fahliyan and deep Gadvan intervals. This overpressure was explicitly incorporated into stress polygon analyses by adjusting effective stresses, thereby increasing accuracy in S_{Hmax} and S_{hmin} determination. In order to identify strike-slip and normal faulting regime, the pore pressure values were included in equations such that the frictional strength comparison used effective stresses. In formations with significant overpressure, such as Well-11's Fahliyan, mud weight selection and fracture initiation pressures in the models reflected the elevated pore pressure, ensuring realistic geomechanical interpretations.

The vertical stress (S_V) magnitude is calculated using the overburden weight (Jaeger and Cook, 1979):

$$S_V = \int_0^z \rho(z) g dz \approx \bar{\rho} g z \quad (1)$$

where z is depth, $\rho(z)$ is rock density as function of depth, g is Earth's gravity acceleration and $\bar{\rho}$ is overburden average density. For logged intervals, density values were taken directly from the wireline density log. In the upper interval above the top of the available density log (unlogged section), density values were estimated from cuttings sample descriptions by assigning representative densities corresponding to the identified lithologies (e.g., marl, sandstone, limestone). These estimated densities were then used to extend the integration to the surface, ensuring a continuous S_V profile.

In addition to the direct formation pressure measurements derived from the MDT tool, a continuous pore-pressure profile was generated using the Eaton method to provide a calibrated pore-pressure curve for comparison with measured data. The Eaton equation (Eaton, 1975) integrates petrophysical log responses with vertical stress derived from overburden density and the normal compaction trend of the sediments. Pore pressure was estimated according to:

$$P_P = S_v - \left(S_v - P_{hyd}\right)(DT_{NCT}/DT)^n \quad (2)$$

where, P_P = pore pressure, S_V = magnitude of vertical stress, P_{hyd} = hydrostatic pore pressure gradient, DT = slowness of compressional wave, DT_{NCT} = normal compaction trend of the sediments and n: Eaton's Exponent. An Eaton exponent of 0.2 was selected for calibration against the MDT pressure points to generate a calibrated pore pressure curve.

Mechanical rock parameters, including static Young's modulus (E), unconfined compressive strength (UCS), cohesion (c), and internal friction angle (ϕ), were obtained from laboratory measurements. Core plug samples were tested under uniaxial and triaxial (multistage) compression to obtain discrete values of these parameters following ASTM D3148–93 and ASTM D2664-95a standards.

The direct laboratory measurements on core plugs provide supporting data for rock strength characterization. Fig. 5 shows an example of a UCS test performed on a representative Fahliyan sample; it displays the stress–strain response. A summary of all uniaxial tests conducted on Gurpi, Gadvan, and Fahliyan cores is provided in Table 3, which includes the derived UCS values together with the corresponding elastic parameters. The triaxial compression measurements used to derive depth-dependent cohesion and friction angle are summarized in Table 4. The

Table 2
Summary of well inclination and azimuth of wells data used for stress feature detection.

Well name	Image log type	Inclination, °	Azimuth, °	Stress features identified
Well-01	Electrical	1.2	28	Breakout
Well-02	Electrical	1.4	159	Breakout
Well-03	Electrical	1.5	132	Breakout
Well-04	Electrical	1.6	1	Breakout
Well-05	Ultrasonic	3.8	99	Breakout
Well-06	Electrical	1.7	122	Breakout
Well-07	Electrical	1.3	151	Breakout
Well-08	Electrical	2.4	129	Breakout
Well-09	Electrical	3.1	197	Breakout
Well-10	Electrical	2.5	160	Breakout
Well-11	Electrical	1.7	289	Breakout & induced fracture

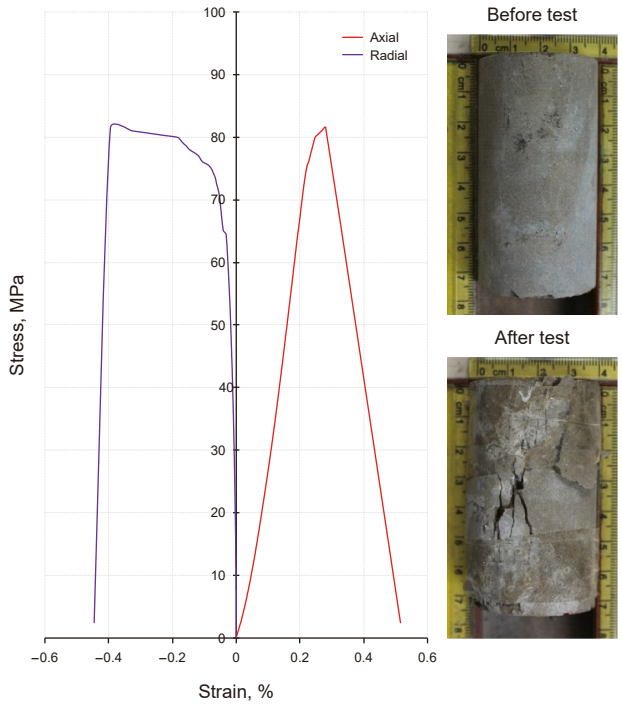

Fig. 5. Representative UCS test on a Fahliyan core plug showing axial and radial stress–strain curves together with the sample condition before and after failure.

Table 3
Laboratory-measured uniaxial compressive strength (UCS), Young's modulus (E), and Poisson's ratio (ν) for core samples from the Gurpi, Gadvan, and Fahliyan formations across Wells 10, 09, and 11.

Well	Formation	Depth, m	UCS, MPa	E, GPa	ν
Well-10	Gurpi	2205.5	39.7	31.3	0.23
		2218.9	46.3	34.1	0.24
		2228.5	47.6	34.5	0.24
Well-09	Gadvan	3859.8	73.9	34.3	0.21
		3876.6	38.1	30.9	0.22
		3893.4	43.5	33.1	0.23
		3901.1	42.2	31.4	0.24
Well-11	Fahliyan	4157.3	81.4	42.9	0.21
		4167.4	69.3	38.7	0.23
		4185.2	81.5	41.7	0.21
		4238.9	65.9	36.1	0.23
		4264.6	48.4	29.5	0.25

triaxial measurements supply the confining-pressure-dependent strength envelope and constitute the basis for determining the cohesion (c) and friction angle (ϕ) that were used in the geomechanical model.

Breakouts and induced fractures in the wellbore, especially from image logs, provide the data to determine the orientation of horizontal stresses and estimate their magnitude (Dasgupta et al., 2019; Davari et al., 2025). The wireline logs are essential tools for in-situ stress analysis tools, yielding a continuous and high-resolution method of estimating stress magnitudes, a technique routinely blended with acoustic emission (AE) testing (Lai et al., 2024). This data is critical as the knowledge of the three principal elements of stress—vertical stress, minimum horizontal stress, and maximum horizontal stress, along with pore pressure—is one of the keys to hydraulic fracturing optimization and safe directional drilling (Lai et al., 2024). Both electrical and ultrasonic types of image logs were employed in this study depending on the availability of wells, with FMI/XRMI logs containing high-resolution electrical

Table 4
Summary of laboratory-derived friction angle (ϕ) and cohesion (c) values for Gurpi, Gadvan, and Fahliyan formations across Wells 10, 09, and 11.

Well	Formation	Depth, m	ϕ, °	c, MPa
Well-10	Gurpi	2204.9	33.1	18.2
		2219.5	34.9	18.9
		2229.5	35.3	21.7
Well-09	Gadvan	3860.9	33.4	20.2
		3878.3	29.8	17.8
		3893.2	30.2	15.2
		3907.4	31.5	16.1
Well-11	Fahliyan	4157.2	29.9	15.9
		4169.5	32.5	16.3
		4240.1	33.5	18.2
		4254.5	28.7	13.3

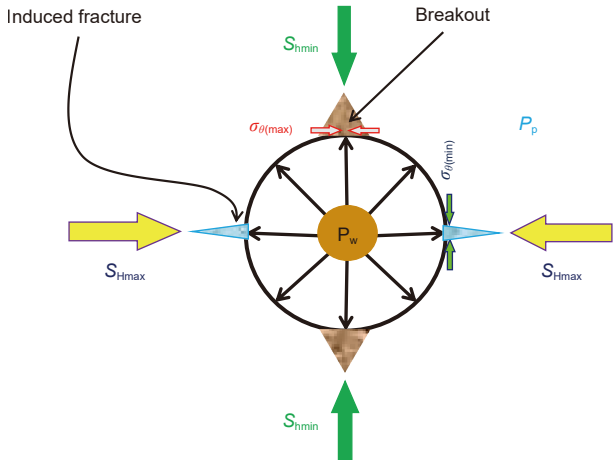

Fig. 6. Borehole breakouts and drilling-induced fractures (DIFs) reveal in-situ stress orientations. Breakouts, aligned S_{hmin}, indicate compressive failure. DIFs, parallel to the S_{Hmax}, signify tensile failure (modified after Abedifar and Abdideh, 2017).

resistivity contrasts and UBI logs having full borehole wall acoustic images. During drilling the material is removed and the surrounding rock loses support and gets stressed near the wellbore wall. Borehole breakout occurs when the circumferential stress around a wellbore exceeds the formation's compressive strength and breakouts form along S_{hmin} (Fig. 6). When these stresses exceed the compressive failure threshold borehole breakouts occur and the wellbore expands as the shear planes intersect and fragments detach from the wall. On the other hand Drilling Induced Fractures (DIFs, Chatterjee and Mukherjee, 2023) occur when the stress around a borehole exceeds the tensile strength of the rock in the wellbore wall and form narrow, well defined fractures that run parallel or slightly oblique to the borehole axis in vertical wells (Fig. 6). Unlike other fractures, DIFs do not enlarge the borehole in the direction of the fracture and align with S_{Hmax} (Zoback, 2010).

Using stress polygon along with breakouts and induced fractures identified from image logs is one of the approaches to estimating the magnitude of horizontal stresses. The stress polygon concept, developed by Zoback et al. (1986) and furthered by Moos and Zoback (1990), serves as a visualization tool to understand the interplay between overburden stress and the horizontal stresses (both maximum and minimum) at a specific depth, given a known pore pressure and an assumed friction coefficient (as noted by Enderlin (2008)). These polygons illustrate the range of possible stress values at that depth and can also indicate the stability of a fault within the current stress environment if the principal stress values are available.

The Earth's crust contains numerous faults and discontinuities (Mukherjee, 2021; Mukherjee et al., 2025), which affect stress magnitudes at depth. Importantly, the difference between the maximum and minimum principal stresses is constrained by the frictional strength of these faults. Stress magnitudes in the crust can be predicted from this relationship without exceeding the frictional strength of existing faults, suggesting that stress states are maintained in equilibrium with this strength in many regions. Jaeger and Cook (1979), demonstrated that the values of σ_1 (minimum effective stress) and σ_3 (maximum effective stress) applicable to a scenario where a critically oriented fault reaches its frictional limit can be expressed as:

$$\sigma_1 / \sigma_3 = (S_1 - P_P) / (S_3 - P_P) = \left[\left(\mu^2 + 1\right)^{1/2} + \mu\right]^2 \quad (3)$$

Such that for $\mu = 0.6$,

$$\sigma_1 / \sigma_3 = 3.1 \quad (4)$$

where σ_1 = maximum principal stress, σ_3 = minimum principal stress, P_P = pore pressure and μ = friction coefficient (Zoback, 2010). The frictional strength of pre-existing faults limits the difference between σ_{Hmax} and σ_{hmin}. Faults that are optimally oriented slip as S_{Hmax} increases relative to S_{hmin}, while those oriented nearly orthogonally to S_{Hmax} cannot slip due to excessive normal stress. Faults striking sub-parallel to S_{Hmax} experience low normal and shear stresses. By using Eq. (1) and Anderson's faulting theory (Anderson, 1905), one can determine the correspondence between maximum and minimum effective stresses and the principal stresses in various faulting environments (Zoback, 2010).

Normal faulting:

$$\sigma_1 / \sigma_3 = (S_V - P_P) / (S_{hmin} - P_P) \leq \left[\left(\mu^2 + 1\right)^{1/2} + \mu\right]^2 \quad (5)$$

Strike-slip faulting:

$$\sigma_1 / \sigma_3 = (S_{Hmax} - P_P) / (S_{hmin} - P_P) \leq \left[\left(\mu^2 + 1\right)^{1/2} + \mu\right]^2 \quad (6)$$

Reverse faulting:

$$\sigma_1 / \sigma_3 = (S_{Hmax} - P_P) / (S_V - P_P) \leq \left[\left(\mu^2 + 1\right)^{\frac{1}{2}} + \mu\right]^2 \quad (7)$$

The placement of horizontal stresses within the triangular areas of the polygon corresponds to different stress regimes, such as normal, strike-slip, and reverses faulting. When the horizontal stresses are positioned at the edge of the polygon, it signifies that a Mohr circle is in contact with the failure line, placing the minimum horizontal stress and effective vertical stress at values that indicate the fault is critically stable. For a normal faulting scenario, the vertical stress represents the maximum principal stress, where the maximum horizontal stress is less than or equal to vertical stress, and the minimum horizontal stress must exceed a threshold determined by the frictional strength of the crust (Taghipour et al., 2019; Ezati et al., 2019; Baouche et al., 2020; Zhang et al., 2021; Sundli et al., 2024). Fig. 7 illustrates an example of a stress polygon along with the necessary equations for delineating its various regions.

Two LOT data sets were used to determine the magnitude of minimum horizontal stress. A schematic pressure-time history for an LOT illustrates that when a constant pumping rate is maintained, the pressure in the wellbore should increase linearly over time (Fig. 8). However, when there is a noticeable departure from this linear increase, known as the leak-off point (LOP), it indicates

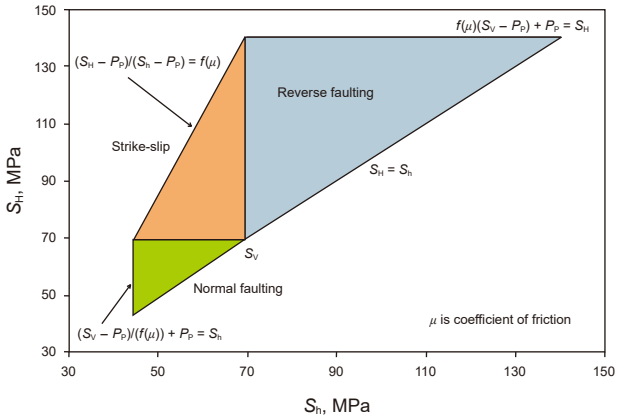

Fig. 7. The stress polygon visualizes the relationship between overburden stress and horizontal stresses, illustrating regions of stability for different faulting regimes, including normal, strike-slip, and reverse faulting (modified after Taghipour et al., 2019).

that a hydraulic fracture has formed. This occurs because a significant increase in system volume is necessary to cause a decrease in the rate of wellbore pressurization, meaning the pressure must be sufficient to propagate the fracture away from the wellbore. The LOP is approximately equal to the least principal stress, although factors such as the tortuosity of the perforation system or high viscosity fluids can cause the pressure to exceed this value (Zoback, 2010).

The LOT performed at the Gurpi Formation provides a direct constraint on the minimum principal stress. As shown in Fig. 9, wellhead pressure increases linearly with pumped volume up to 2630 psi, after which a sudden pressure drop marks the onset of formation breakdown and fracture propagation. This observation documents a breakdown pressure of 2630 psi, a total pumped volume of 10.5 bbl, and an abrupt deviation from linearity due to the brittle response of the argillaceous limestone. During the test, the mud weight in the wellbore was 76 pcf, and therefore estimation of the minimum horizontal stress magnitude needs to take

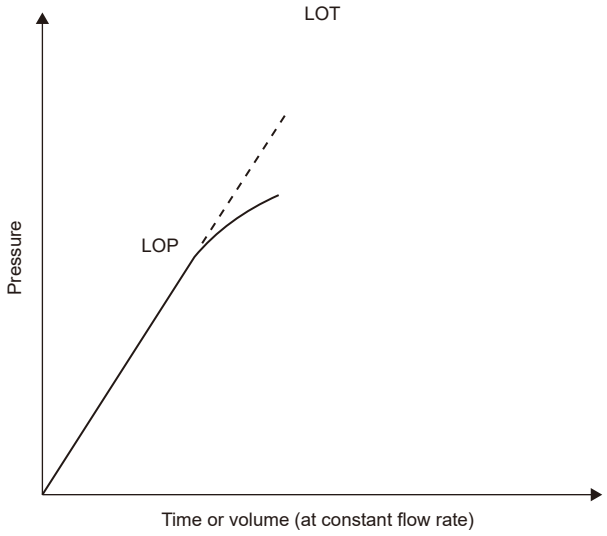

Fig. 8. This figure illustrates the pressure-time relationship during an LOT, highlighting key points such as the leak-off point (modified after Gilchrist et al., 2020).

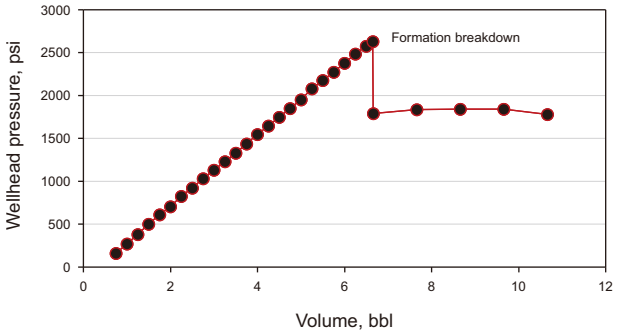

Fig. 9. Pressure–volume plot from the leak-off test (LOT) conducted in Well-10, showing a linear increase in wellhead pressure up to 2630 psi, followed by a sharp drop indicating formation breakdown and fracture propagation.

into consideration both the hydrostatic mud column pressure at the casing shoe depth and the recorded surface pressure.

The LOT conducted in Well-09 in the Gadvan Formation provides a key data on the magnitude of minimum horizontal stress. As presented in Fig. 10, the pressure–volume response shows a linear trend up to the onset of deviation, marking the leak-off point at 2.4 of pumped volume and a surface pressure of 2300 psi. During the test, the mud weight in the wellbore was 100 pcf. The LOP observed represents the start of tensile failure in the Gadvan Formation.

Worked example for strike-slip faulting, given the following data:

- Pore pressure (P_P) = 28.11 MPa
- Vertical stress (S_V) = 49.43 MPa
- Minimum horizontal stress (S_{hmin}) = 39.01 MPa
- Maximum horizontal stress (S_{Hmax}) = 62.10 MPa
- Friction coefficient (μ) = 0.6

We will calculate the stress ratio (σ_1/σ_3) for a strike-slip faulting scenario using the following equation:

$$\sigma_1 / \sigma_3 = (S_V - P_P) / (S_{hmin} - P_P) \quad (8)$$

Plug in the values:

$$\sigma_1 / \sigma_3 = (62.10 - 28.11)/(39.01 - 28.11)$$

$$\sigma_1 / \sigma_3 = 33.99/10.90 \approx 3.1$$

Compare with the frictional strength equation, The frictional strength equation for strike-slip faulting is:

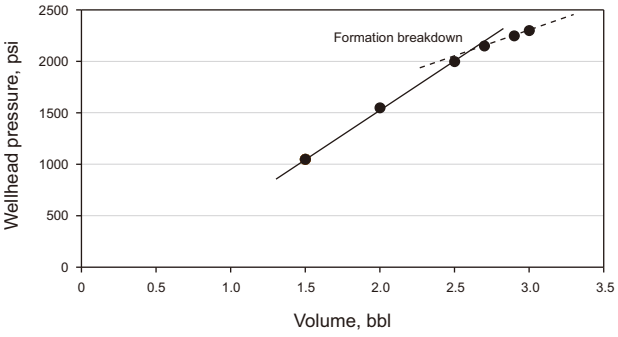

Fig. 10. Pressure–volume plot of the LOT conducted in Well-09 (Gadvan Formation) showing the leak-off point.

$$\sigma_1 / \sigma_3 = \left[\left(\mu^2 + 1\right)^{1/2} + \mu\right]^2 \quad (9)$$

Substituting $\mu = 0.6$ into the equation:

$$\sigma_1 / \sigma_3 = \left[\left(0.6^2 + 1\right)^{1/2} + 0.6\right]^2$$

$$\sigma_1 / \sigma_3 = (1.766)^2 \approx 3.1$$

The calculated value for the stress ratio is approximately 3.1, which matches the value obtained from the frictional strength equation. This confirms that the stress state is consistent with strike-slip faulting. The horizontal stress distribution indicates that the fault is critically stable, meaning it is close to slipping under the given stress conditions.

In addition to using LOT measurements to anchor the minimum horizontal stress and applying the stress-polygon approach to constrain the admissible range of S_{Hmax}, continuous depth-dependent profiles of S_{hmin} and S_{Hmax} were also estimated using the poroelastic equations of Fjaer et al. (2008).

$$S_{hmin} = \frac{\nu}{(1-\nu)}(S_V - \alpha P_P) + \alpha P_P + \frac{E}{(1-\nu^2)}\varepsilon_x + \frac{\nu \times E}{(1-\nu^2)}\varepsilon_y \quad (10)$$

$$S_{Hmax} = \frac{\nu}{(1-\nu)}(S_V - \alpha P_P) + \alpha P_P + \frac{E}{(1-\nu^2)}\varepsilon_y + \frac{\nu \times E}{(1-\nu^2)}\varepsilon_x \quad (11)$$

where ν is Poisson's ratio, S_V is vertical stress, α is Biot's coefficient, P_P is pore pressure and E is Young's modulus and the tectonic strain on x (ε_x) and y (ε_y) axes. In the calculations, a tectonic strain of ε_x = 0.05 millistrain and ε_y = 0.59 millistrain was applied.

3.3. Uncertainty analysis

The Stress Polygon method is useful for estimating maximum horizontal stress but involves several uncertainties. Key issues include errors in input data like stress measurements, assumptions of a uniform stress field, and subjective interpretation when forming the polygon. These factors can lead to inaccurate stress estimates, highlighting the importance of careful data selection and analysis.

The uncertainty in geomechanical tests like UCS and triaxial tests arises from factors such as equipment calibration, operator error, and sample heterogeneity. For UCS testing, the coefficient of variation (CV) for homogeneous rock specimens is typically less than 25%, resulting in errors between 5% and 15% (Bewick et al., 2015). Therefore, the average potential error percentage for the UCS test results will be 10%. Based on the stress analysis of the polygon, considering a 10% error in the UCS test results, the stress calculations will include a 3.4% uncertainty.

The use of XLOT or minifrac data, would help to reduce uncertainty in these estimations and offer a more complete picture of the stress magnitudes. Therefore, while the LOT data used in this study is informative, the availability of additional XLOT or minifrac measurements would further enhance the accuracy and reduce uncertainty in the stress analysis. Additionally, increasing the number of stress measurement points would further contribute to reducing uncertainty.

It was assumed that the fracture height during the LOT was confined within the wellbore section, which is critical for accurate stress estimation. However, uncertainties arising from factors such

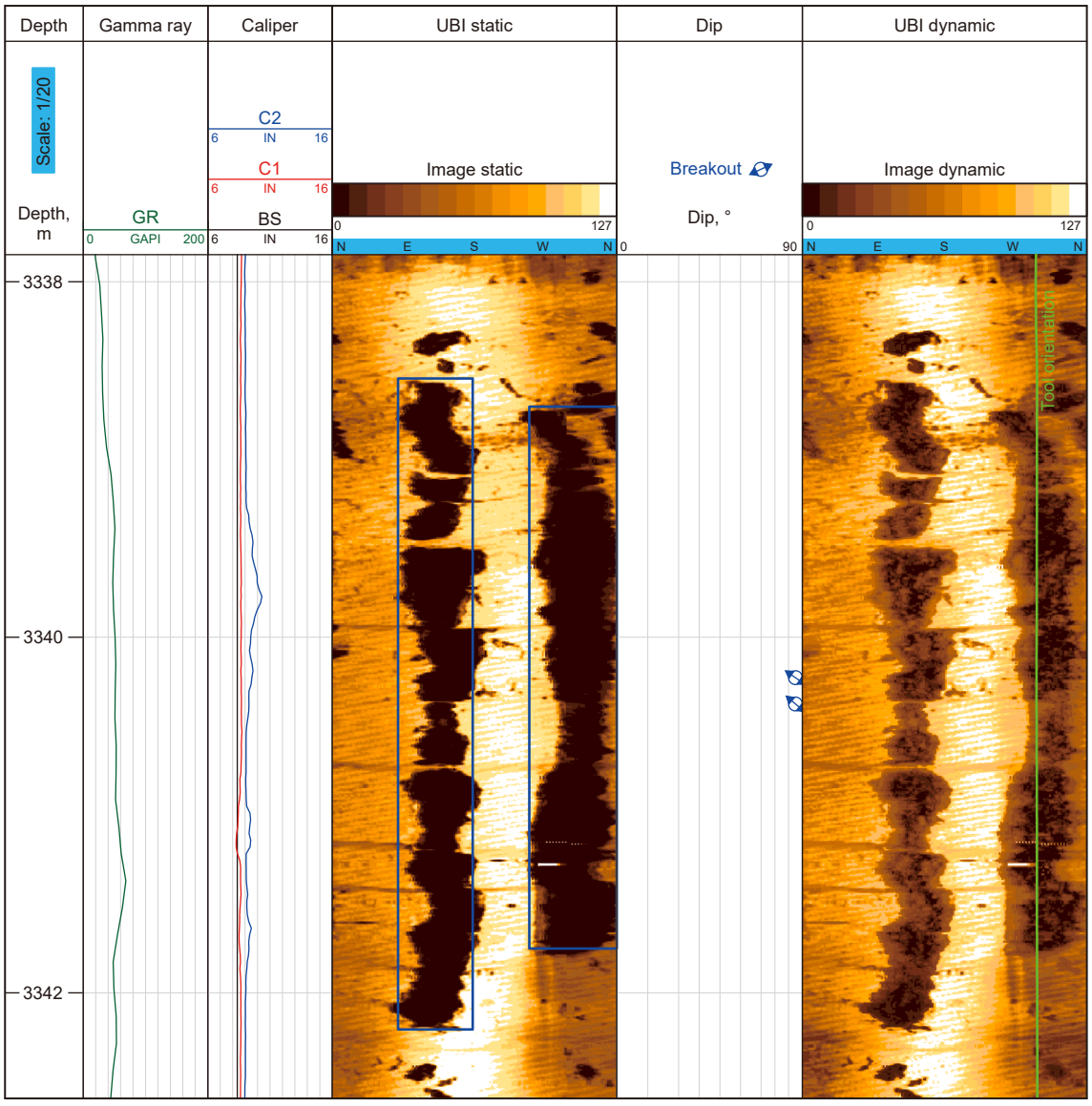

Fig. 11. An example of identified breakouts using UBI image log. A pair of breakouts is displayed on the static image with blue boxes. In addition to the image log, the caliper logs also confirm the existence of breakouts in this interval. This figure is related to the Well-05 of this study.

Table 5
The quantity of breakouts and the orientation of minimum and maximum horizontal stresses in all wells based on image logs.

Well name	Breakout No.	S_{hmin} direction	S_{Hmax} direction (breakout–based)
Well-01	126	N47W-S47E	N43E-S43W
Well-02	32	N47.5W-S47.5E	N42.5E-S42.5W
Well-03	32	N42.5W-S42.5E	N47.5E-S47.5W
Well-04	300	N35W-S35E	N55E-S55W
Well-05	599	N39.5W-S39.5E	N50.5E-S50.5W
Well-06	296	N24W-S24E	N66E-S66W
Well-07	158	N29.5W-S29.5E	N60.5E-S60.5W
Well-08	60	N35W-S35E	N55E-S55W
Well-09	46	N24.5W-S24.5E	N65.5E-S65.5W
Well-10	24	N51.5W-S51.5E	N38.5E-S38.5W
Well-11	54	N39.5W-S39.5E	N50.5E-S50.5W

as rock heterogeneity, and pressure measurement accuracy are acknowledged. To address these uncertainties, additional data sources, including borehole image logs and geomechanical parameters, were integrated to enhance the stress analysis. Potential errors due to the lack of direct fracture height measurements are also likely, and supplementary data such as XLOT or minifrac tests are necessary and essential for refining stress magnitude estimates and reducing uncertainty.

4. Results and discussion

The analysis used multiple data sources to determine the in-situ stress state. Borehole image logs provided the key information to identify wellbore failures which are sensitive indicators of the stress field. The wellbore failures combined with LOT data were used to constrain the maximum horizontal stress. Also, the maximum horizontal stress possible range was estimated using polygon stress analysis.

The stress polygon method which uses data from multiple sources and incorporates geological knowledge and empirical relationships was used to constrain the possible S_{Hmax} values. This method accounts for the uncertainties and ambiguities in the data.

Table 6
Number of breakouts in each formation.

Formation	Breakout No.	Well	Breakout concentration (per well/per formation)
Asmari	96	6	96
Pabdeh	48	6	48
Gurpi	143	4, 5, 6, 7, 8	28.6
Ilam	121	4, 5, 6, 7, 8, 10	20.1
Lafan	12	4,5,6,7,8,10	2
Sarvak	677	1, 2, 3, 4, 5, 6, 7, 8, 9, 10	67.7
Kazhdumi	364	1, 4	182
Dariyan	126	4, 5	63
Gadvan	90	4	22.5
Fahliyan	50	11	50

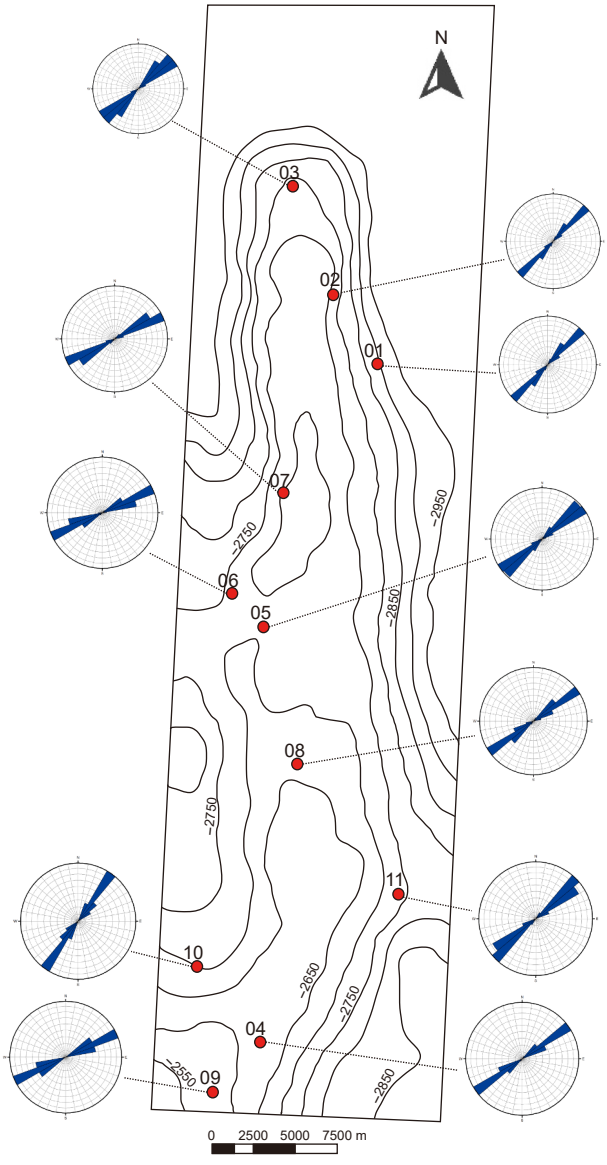

Fig. 12. The rose diagrams used to determine maximum horizontal stress in wells through breakout analysis indicate that, according to image log interpretations from all wells, the direction of maximum horizontal stress is oriented NE-SW.

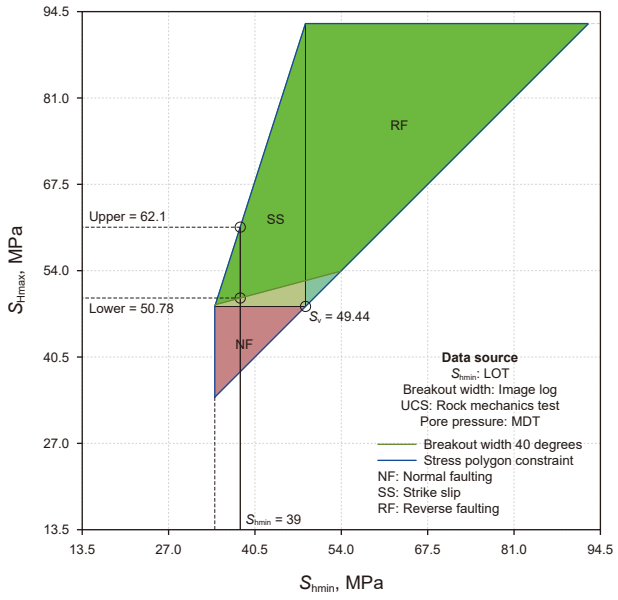

Fig. 13. The stress polygon constructed using LOT data from Well-10 in the Gurpi Formation, highlighting the minimum horizontal stress of 39 MPa and the estimated range of maximum horizontal stress between 50.78 and 62.1 MPa.

To validate the outputs from the geomechanical modeling and add more confidence to the results, seismic data were added to the analysis.

Breakouts are seen in all 11 wells and all formations with a total of 1727 breakouts. Examples of breakouts in Well-05 are shown in Fig. 11. The clarity and detail of these breakouts are more pronounced in the Ultrasonic Borehole Imaging (UBI) image log where the full wellbore wall is imaged and shown in (Fig. 11). To improve the accuracy and efficiency of breakout identification, additional data from tool calipers in the image logs are used (Fig. 11). These calipers provide more measurements and complement the visual data from the UBI logs to give a more complete picture of the wellbore.

The information presented in Table 5 details the number of breakouts seen in the different wells, along with their specific orientations and the corresponding direction of maximum horizontal stress. Particularly, the data show that the direction of S_{Hmax} remains largely consistent across all the wells analyzed. This consistency proposes a well-defined stress field in the region, with the majority of the wells showing orientations that predominantly align in a northeastern to southwestern (NE-SW) direction.

Image logs are often taken from the Sarvak reservoir, considered the most important reservoir in the Abadan Plain area. Out of a total of 10 wells in this reservoir, 677 breakouts have been identified, indicating an average of 67.7 breakouts per well. For the Asmari Formation, only one well has identified 96 breakouts, indicating a high breakout density in this formation. This formation is primarily composed of sandstone that is poorly cemented, which results in low rock strength and makes it prone to breakout formation. Additionally, the Kazhdumi Formation, due to its marl lithology and low rock strength, shows a high density of breakouts (Table 6).

The UGC (Underground contour) map (Fig. 12) shows the direction of S_{Hmax} in the oilfield. Each well's data points to a consistent pattern in the direction of S_{Hmax}, which is inclined relative to the axis of the anticline. S_{Hmax} direction analysis shows

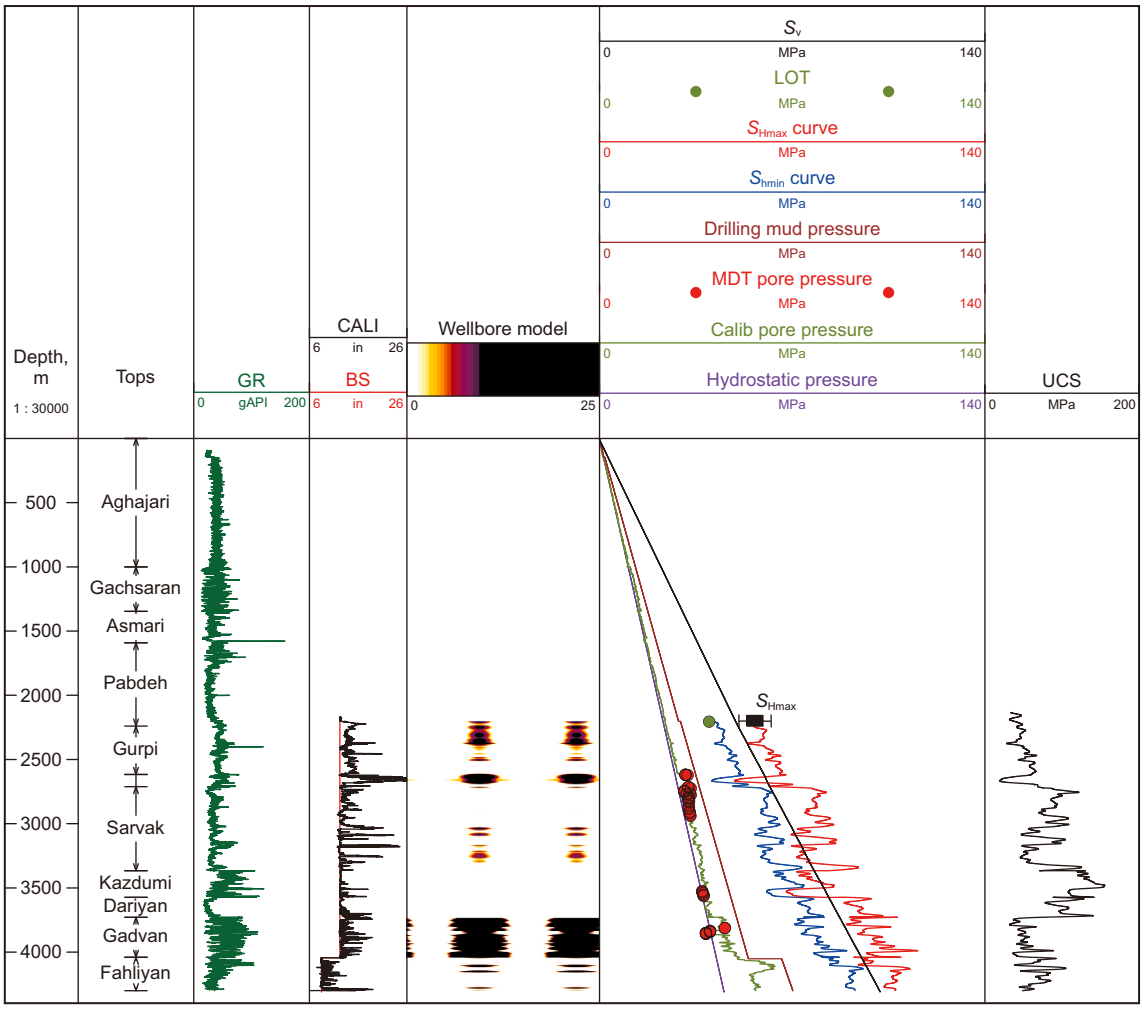

Fig. 14. Pressure and stress data in the Well-10. The plot shows, zonation, Gamma Ray, Caliper-bit sze, modeled wellbore breakouts, hydrostatic pressure, pore pressure, drilling mud pressure, LOT data, S_V, horizontal stresses (S_{Hmax} and S_{hmin}) and UCS. The observed stress regime ($S_{Hmax} > S_V > S_{hmin}$) is consistent with a strike-slip stress state.

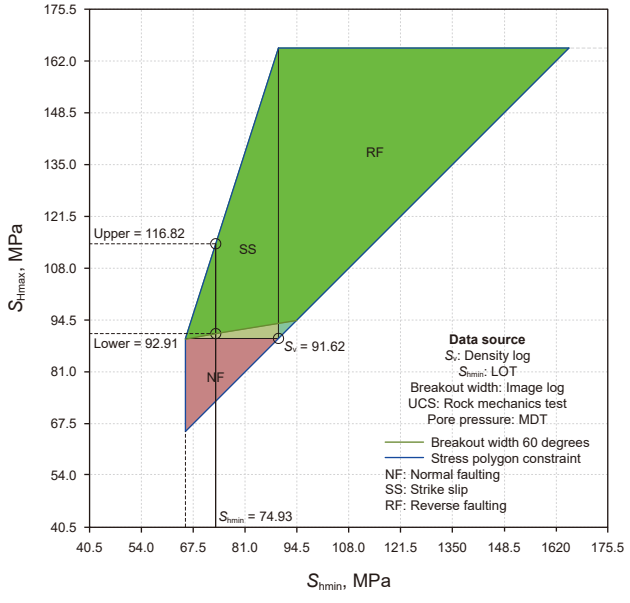

Fig. 15. Stress polygon for Well-09 at the base of the Gadvan Formation, incorporating LOT data and refined through pore pressure measurements, UCS values, and borehole image logs. S_{Hmax} estimates range between 92.91 and 116.82 MPa, reflecting the strike-slip stress state.

that it is aligned with Zagros S_{Hmax} direction, so the principal stress direction in Abadan Plain is the same as Zagros, both are NE-SW (Fig. 12).

This means that the tectonic stresses in Abadan Plain are the same as the Dezful embayment oilfields. So regional tectonics controls the stress regime, geological features and seismicity in the area. This shows that regional geological structures are connected and responding to the current tectonic stresses.

In addition to the stress directions, the magnitudes were also calculated using the available geomechanical, petrophysical, reservoir, and geological information for the study area. This multi-faceted approach gives a better understanding of the current stress state of the area.

Well-10 at the top of the Gurpi Formation has LOT data which is a key to the analysis of subsurface stress. The analysis of the LOT data shows that the minimum horizontal stress in the Gurpi Formation at Well-10 is 39 MPa, so this is the baseline for the stress state (Fig. 13).

To build the stress polygon further, additional parameters were considered, including pore pressure, UCS and image logs. These add more detail to the stress distribution in the formation. The image log shows a breakout of 40° which is important for the estimation of maximum horizontal stress range. This breakout width is the response of the rock to the applied stresses and is a

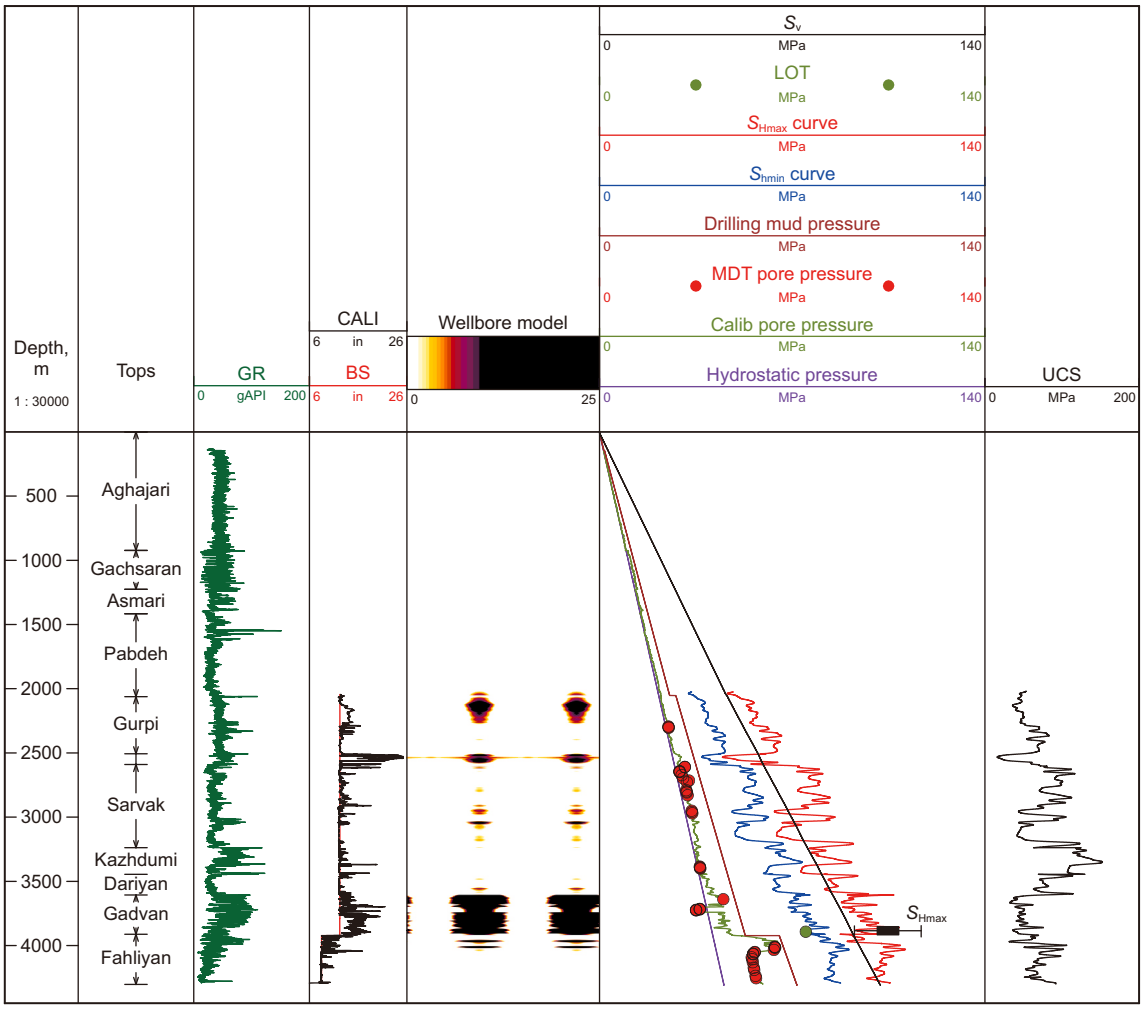

Fig. 16. Pressure and stress conditions in Well-09 of the Gadvan Formation, illustrating S_V with a 1 psi/ft gradient. The stress regime indicates strike-slip stress regime, with S_{Hmax} exceeding S_V and S_{hmin} below S_V.

key to understanding the mechanical behavior of the formation. Accordingly, the maximum horizontal stress was estimated to fall within the range of 50.78–62.1 MPa (Fig. 13).

Fig. 14 shows the various pressure parameters and stress conditions in Well-10 of the Gurpi Formation. It shows the hydrostatic pressure which is the baseline to understand the pore pressure in the subsurface and the pore pressure points which are the pressure exerted by the fluids in the rock pores. Also shown is the drilling mud column pressure which is the pressure exerted by the drilling fluid used during drilling. The LOT data in the figure is important to evaluate and understand the current stress state. The vertical stress is also shown to understand the weight of the overlying rock and its effect on the stress regime.

From the model output, the pore pressure is higher than the hydrostatic pressure. This overpressure is managed by selecting a mud weight higher than the maximum pore pressure encountered. This will keep the formation pressure inside the wellbore and prevent well control issues such as kicks or blowouts. The vertical stress gradient from the model is approximately 1 psi/ft which is a typical value for many sedimentary basins (Fig. 14).

The analysis shows a stress regime in the Gurpi Formation with S_{Hmax} greater than S_V and S_{hmin} less than S_V ($S_{Hmax} > S_V > S_{hmin}$). This inequality is shown in Fig. 14 and is an indicator of strike-slip stress regime. Additionally, it can be noted that the lower bound of the probable range for S_{Hmax} is close to S_V, so it can be considered a type of strike-slip normal stress state.

To provide a continuous and integrated view of the in-situ horizontal stresses, S_{hmin} and S_{Hmax} were estimated along the logged interval using the poroelastic approach and then calibrated with available LOT measurement (Fig. 14). Then the continuous stress profiles utilized for the wellbore-failure model construction. Comparison of the modeled failure zones with caliper enlargements shows a consistent pattern, indicating that the integrated stress interpretation offers a coherent and depth-continuous representation of the stress conditions across the well.

Subsurface stress analysis at Well-09 at the base of the Gadvan Formation used LOT data as the main constraint for the stress polygon (Fig. 15). The LOT data gave a S_{hmin} of 74.93 MPa which gave us a good understanding of the in-situ stress regime in the formation. This was further refined by integrating multiple data sources including pore pressure measurements, UCS from core analysis and detailed borehole image logs.

The borehole image logs show the 60-degree breakout width in this well which is a well-established indicator of S_{Hmax} direction and magnitude and narrowed down the range of possible S_{Hmax} magnitudes. This integrated approach gave us a S_{Hmax} range of 92.91–116.82 MPa (Fig. 15). The range highlights the need for a multi-disciplinary approach combining different data types to

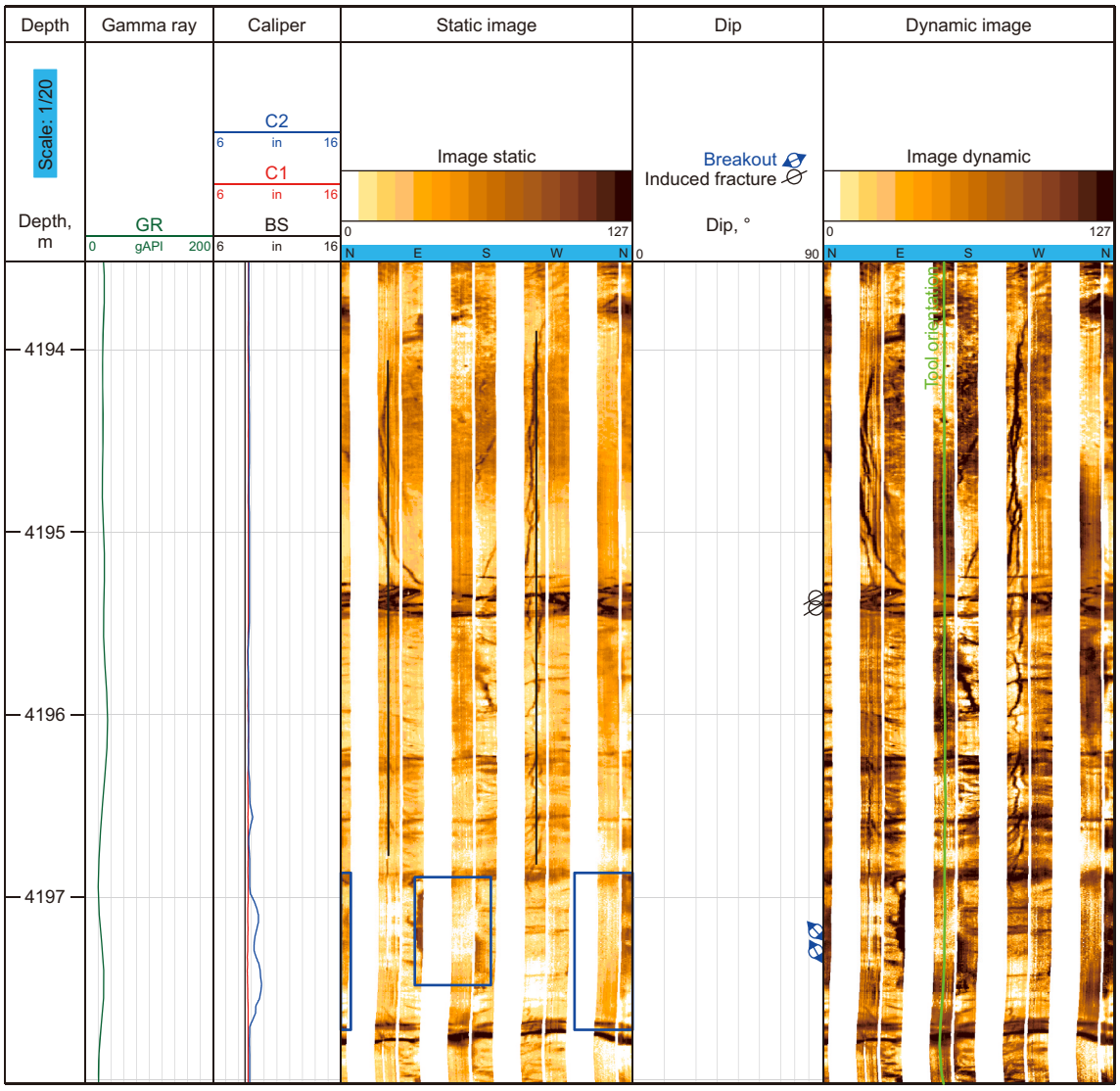

Fig. 17. The simultaneous occurrence of breakout and induced fractures in Well-11, Fahliyan Formation. The breakouts are indicated by blue boxes and induced fractures are marked with black lines. See Chakraborty and Mukherjee. (2020) for interpretation of unrolled images.

constrain the stress tensor and ultimately improve the subsurface stress model for Well-09.

Fig. 16 shows the pressure and stress conditions in Well-09 of the Gadvan Formation. The model shows the pore pressure is above hydrostatic and similar to Well-10 with 1 psi/ft S_V gradient. Like Well-10 in the Gurpi Formation, the Gadvan Formation has a stress regime where S_{Hmax} is above S_V and S_{hmin} is below S_V. As shown in Fig. 16 this is a strike-slip stress regime. But the lower limit of the likely range for S_{Hmax} is near S_V, which means it can be regarded as a form of strike-slip normal stress state.

The integrated log display in Fig. 16 shows that borehole enlargements cluster within the Gurpi, Ilam, Gadvan, and Fahliyan formations, where the caliper signatures exhibit typical breakout geometries. The modeled wellbore failure predicts the same depth ranges as prone to shear failure, demonstrating a close match between observed breakouts and the wellbore-failure model across the formations.

In the FMI log of well-11 both borehole breakout and drilling induced fractures are seen together (Fig. 17). The presence of both breakout and induced fractures in an interval is a geomechanical key data point that shows significant difference in horizontal stresses and is very useful for polygon stress analysis.

Fig. 17 shows the Fahliyan Formation which has higher pore pressure than the overlying formations. Due to this higher pore pressure, the Fahliyan Formation should be drilled with heavier mud weight of 110 pcf, which consequently increases the likelihood of inducing fractures in this formation. Furthermore, in well-11, the induced fractures reveal a clear alignment with the S_{Hmax} orientation, which is observed to be in a northeast-southwest direction.

Due to the lack of LOT data in well-11, direct determination of the minimum horizontal stress using conventional methods is not possible. But presence of both breakouts and induced fractures in the same interval provided alternative data to estimate stress state. These wellbore failure events are valuable to infer stress magnitude. The intersection of the breakout width range and the induced fracture on the stress polygon (Fig. 18) defines a region within which the S_{hmin} and S_{Hmax} magnitudes should be.

The observed breakout width in Well-11 ranged from 70° to 90°. Furthermore, the tensile strength of the rock, measured at

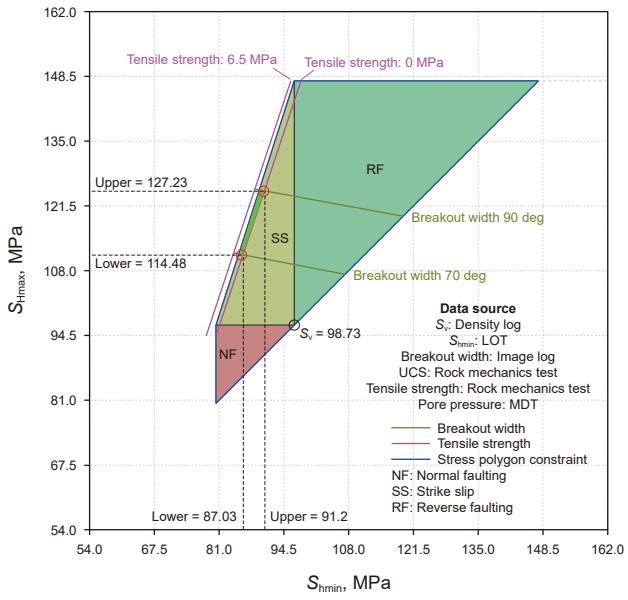

Fig. 18. Absence of LOT data at Well-11 necessitated an alternative stress estimation. Stress state was estimated using 70°–90° breakouts and induced fractures along with the stress polygon analysis.

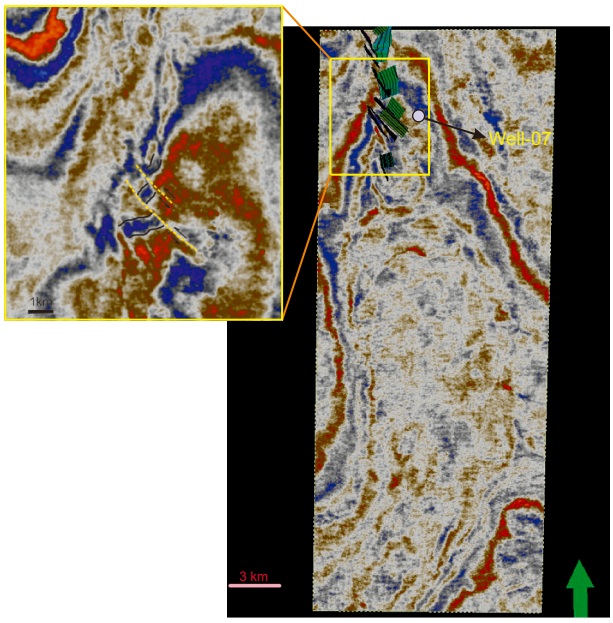

Fig. 20. The identified faults using seismic data in the northwest part of the field mainly show strike-slip mechanisms.

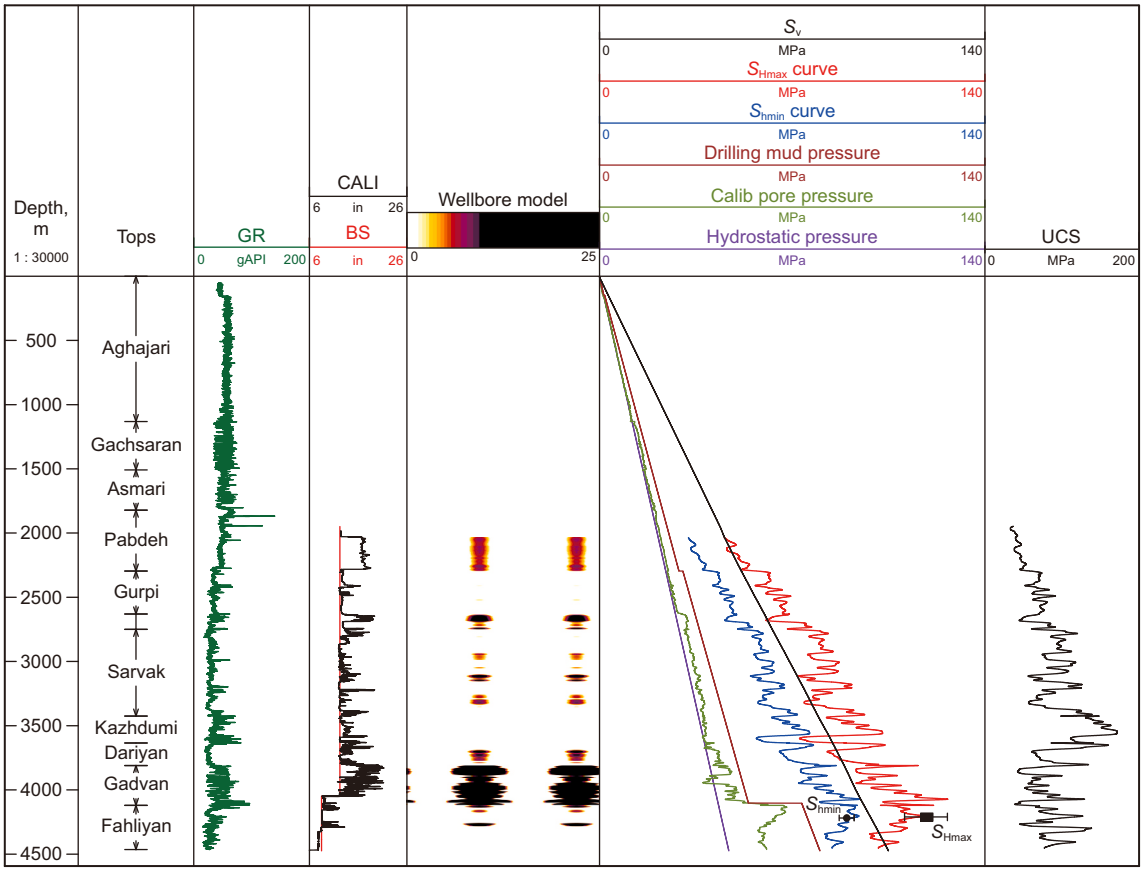

Fig. 19. Well-11 exhibits a strike-slip stress regime ($S_{Hmax} > S_V > S_{hmin}$), consistent with observations in Wells 9 and 10. This supports a regional strike-slip stress regime.

6.5 MPa, was incorporated into the stress analysis to refine the S_{hmin} and S_{Hmax} estimations. Using the data from stress polygon analysis (Fig. 18), it can be observed that the S_{hmin} range is between 87.03 and 91.2 MPa, while the S_{Hmax} range falls between 114.48 and 127.23 MPa.

In Well-11 the stress state analysis shows the minimum horizontal stress is less than the vertical stress across all the ranges. And the maximum horizontal stress is always greater than the vertical stress across all the methods in this well (Fig. 19). This characteristic further supports the categorization of the stress regime as strike-slip, as indicated by the observed patterns in the horizontal stress measurements.

Also, this strike-slip stress regime is not limited to Well-11, it is also seen in Wells 10 and 9, so it's a regional phenomenon. A strike-slip regime means lateral shear forces are playing a big role in the subsurface.

Fig. 19 shows that pronounced enlargements of the borehole occur in the Pabdeh, Sarvak, Gadvan, and Fahliyan formations, because the caliper responses reflect breakout and washout evidences. A close agreement between the observed breakout clusters and failure model outputs suggests that continuous stress profiles capture formation by formation variations in wellbore stability across the entire section.

Fig. 20 shows the faults in the northwestern part of the study area on a seismic time slice. The faults associated with the Jurassic horizon in the field are sinistral strike-slip mechanism, indicating that the movement along these faults is primarily horizontal. The sinistral strike-slip mechanisms can also influence the local stress field which in turn has implications for fault stability and future seismicity. The interpretation of fault movement in this area gives us insight into the past geological history and is a valuable tool for predicting future geological events and making informed decisions for exploration and development in the area.

The observed strike-slip movement along these faults may not necessarily reflect the present-day stress regime, but could instead be the result of paleo-stress conditions that were active during earlier tectonic phases. Seismic interpretation often captures the cumulative structural history of a region, which includes both recent and ancient deformation events. Therefore, while the strike-slip geometry of the faults may suggest compatibility with the current stress state, this alone is not sufficient to confirm ongoing strike-slip activity. To accurately assess whether these faults are still active in a strike-slip regime under present-day stress conditions, additional evidence is required—specifically, focal mechanism analysis from recent seismic events. Such analysis provides direct insight into the current orientation and style of faulting and is essential to validate interpretations based on structural data.

5. Conclusions

The analysis of in-situ stress conditions in the Abadan Plain has provided information about regional stress regime and its usage in reservoir management. The utilization of diversified sources of data—borehole image logs, LOT data, seismic data, and geology—was very important in S_{Hmax} constraining and enhancing the stress state in different formations. The similarity in the orientation of S_{Hmax} in all wells, which is mostly NE–SW-oriented, reflects the existence of a well-defined and regionally consistent stress field.

The simultaneous observation of induced fractures and breakouts in Well-11 imposed additional constraints for stress estimation, enhancing the reliability of the stress model. The incorporation of geomechanical, petrophysical, and geological data enhanced the accuracy of stress magnitude estimations.

The stress polygon method demonstrated that SHmax is larger than the vertical stress, while S_{hmin} is less than the vertical stress, reflecting a strike-slip stress regime consistent in a number of formations and wellbore conditions. Comparisons with earlier studies (Abdollahie Fard et al., 2006) suggest that the stress regime of the Abadan Plain may have evolved from a predominantly normal regime to the current strike-slip regime. However, further dynamic modeling of the geological and geomechanical history is needed to validate this concept.

These results provide additional information of geomechanical behavior in the Abadan Plain, with practical implications for wellbore stability, exploration, and development. Continued integration of multiple datasets and innovative modeling techniques will enable a higher-resolution characterization of the complex stress regimes controlling this region.

CRediT authorship contribution statement

Mohsen Ezati: Writing – original draft, Data curation, Conceptualization. **Ali Kadkhodaie:** Writing – review & editing, Supervision, Methodology, Conceptualization. **Vahid Bolandi:** Validation, Project administration, Methodology, Investigation.

Data availability

All data applied to accomplish this research will be available under reasonable demand.

Funding

This research is supported by the research grant of the University of Tabriz (Grant No. 4830), which we are grateful of.

Declaration of competing interest

The authors declare that they have no known competing financial interests or personal relationships that could have appeared to influence the work reported in this paper.

References

Abbasi, R., Mehrabi, H., Yahyaei, E., Rahimpour-Bonab, H., 2024. Diagenetic evolution of Upper Cretaceous carbonate sequences (Sarvak formation) in the Abadan Plain, Iran: Evidence from petrographic, elemental, stable, and strontium isotopic data. Int. Geol. Rev. 66 (22), 3793–3813. https://doi.org/10.1080/00206814.2024.2361276.

Abdollahie Fard, I., Braathen, A., Mokhtari, M., Alavi, S.A., 2006. Interaction of the Zagros fold–thrust belt and the Arabian-type, deep-seated folds in the abadan Plain and the Dezful Embayment,SW Iran. Pet. Geosci. 12 (4), 347–362. https://doi.org/10.1144/1354-079305-706.

Abedifar, M., Abdideh, M., 2017. Determination OF collapse and fracture pressures for wellbore stability design based on the mogi-coulomb failure criterion. Petrol. Coal 59 (4).

Al-Husseini, M.I., 2000. Origin of the arabian plate structures: Amar Collision and Najd Rift. GeoArabia (Manama) 5 (4), 527–542. https://doi.org/10.2113/geoarabia0504527.

Anderson, E.M., 1905. The dynamics of faulting. Trans. Edinb. Geol. Soc. 8 (3), 387–402. https://doi.org/10.1144/transed.8.3.387.

Assadi, A., Honarmand, J., Moallemi, S.A., Abdollahie-Fard, I., 2023. Impacts of depositional facies and diagenesis on reservoir quality: A case study from the rudist-bearing Sarvak formation, Abadan plain, SW Iran. Acta Geol. Sin. - English Ed. 97 (1), 190–206. https://doi.org/10.1111/1755-6724.14984.

Atashbari, V., Tingay, M., Amrouch, K., 2018. Stratigraphy, tectonics and hydrocarbon habitat of the Abadan plain basin: A geological review of a prolific Middle Eastern hydrocarbon province. Geosciences 8 (12), 496. https://doi.org/10.3390/geosciences8120496.

Baouche, R., Sen, S., Boutaleb, K., 2020. Present day In-situ stress magnitude and orientation of horizontal stress components in the eastern Illizi Basin, Algeria: A geomechanical modeling. J. Struct. Geol. 132, 103975. https://doi.org/10.1016/j.jsg.2019.103975.

Beaumont, C., 1981. Foreland basins. Geophys. J. Int. 65 (2), 291–329. https://doi.org/10.1111/j.1365-246x.1981.tb02715.x.

Bewick, R.P., Amann, F., Kaiser, P.K., Martin, C.D., 2015. Interpretation of *UCS* test results for engineering design. In: ISRM Congress. ISRM-13CONGRESS.
Bondur, V.G., Garagash, I.A., Gokhberg, M.B., Rodkin, M.V., 2016. The evolution of the stress state in southern California based on the geomechanical model and current seismicity. Izvestiya Phys. Solid Earth 52, 117–128.
Cao, D., Zeng, L., Gomez-Rivas, E., Gong, L., Liu, G., Lu, G., Bons, P.D., 2024. Correction of linear fracture density and error analysis using underground borehole data. J. Struct. Geol. 184, 105152.
Chakraborty, M., Mukherjee, S., 2020. Structural geological interpretations from unrolled images of drill cores. Mar. Petrol. Geol. 115, 104241. https://doi.org/10.1016/j.marpetgeo.2020.104241.
Chatterjee, S., Mukherjee, S., 2023. Review on drilling-induced fractures in drill cores. Mar. Petrol. Geol. 151, 106089. https://doi.org/10.1016/j.marpetgeo.2022.106089.
Dasgupta, T., Dasgupta, S., Mukherjee, S., 2019. Image log interpretation and geomechanical issues. In: Springer Geology. Springer, Singapore, pp. 237–251. https://doi.org/10.1007/978-981-13-2781-0_10.
Davari, M.A., Ezati, M., Jafarizadeh, F., Motamedi, M., 2025. Enhancing breakout identification in geomechanical modeling: Using fullset logs with machine learning in carbonate reservoirs. Earth Sci. Info. 18, 81. https://doi.org/10.1007/s12145-024-01641-8.
DeCelles, P.G., Giles, K.A., 1996. Foreland basin systems. Basin Res. 8 (2), 105–123. https://doi.org/10.1046/j.1365-2117.1996.01491.x.
Dickinson, W.R., 1974. Plate Tectonics And Sedimentation. SEPM Society for Sedimentary Geolog. https://doi.org/10.2110/pec.74.22.0001.
Dong, Z., Tian, S., Xue, H., Lu, S., Liu, B., Erastova, V., Wu, M., Wu, R., 2024. Analysis of pore types in lower cretaceous qingshankou shale influenced by electric heating. Energy Fuel. 38 (21), 20577–20590. https://doi.org/10.1021/acs.energyfuels.4c03783.
Eaton, B.A., 1975. The equation for geopressure prediction from well logs. In: SPE Annual Technical Conference and Exhibition. https://doi.org/10.2118/5544-ms. SPE-5544.
Edgell, H.S., 1996. Salt tectonism in the Persian Gulf basin. Geol. Soc. London 100 (1), 129–151. https://doi.org/10.1144/gsl.sp.1996.100.01.10.
Enderlin, M., 2008. The stress polygon: 20 years later, still the tool for evaluating and integrating the scale of stress influence. In: AAPG Search and Discover Article. AAPG Annual Convention, San Antonio, Texas, USA.
Ezati, M., Azizzadeh, M., Riahi, M.A., Fattahpour, V., Honarmand, J., 2020. Wellbore stability analysis using integrated geomechanical modeling: A case study from the Sarvak reservoir in one of the SW Iranian oil fields. Arabian J. Geosci. 13, 1–19. https://doi.org/10.1007/s12517-020-5126-1.
Ezati, M., Azizzadeh, M., Riahi, M.A., Fattahpour, V., Honarmand, J., 2019. Application of DSI log in geomechanical and petrophysical evaluation of carbonate reservoirs: A case study in one of the SW Iranian oil fields. J. Petrol. Res. 29, 37–50. https://doi.org/10.22078/pr.2019.3552.2625.
Ezati, M., Soleimani, B., Moazeni, M.S., 2014. Fracture and horizontal stress analysis of Dalan formation using FMI image log in one of southwestern Iranian oil wells. J. Tethys 2 (1), 1–8.
Fang, T., Ren, F., Wang, B., Hou, J., Wiercigroch, M., 2025. Multi-scale mechanics of submerged particle impact drilling. Int. J. Mech. Sci. 285, 109838. https://doi.org/10.1016/j.ijmecsci.2024.109838.
Fjaer, E., Holt, R.M., Horsrud, P., Raaen, A.M., 2008. In: Petroleum Related Rock Mechanics, second ed. Elsevier.
Gilchrist, C.J., Cosgrove, J.W., Parmassar, K.J., 2020. Critically stressed fractures: Analysis of the Shaikan field, Kurdistan region of Iraq. J. Geol. Soc. 177 (6), 1315–1328. https://doi.org/10.1144/jgs2019-136.
Heidbach, O., Rajabi, M., Reiter, K., Ziegler, M., Wsm Team, 2016. World stress map database release 2016. GFZ Data Serv. 10, 1.
Jaeger, J.C., Cook, N.G.W., 1979. Fundamentals of Rock Mechanics, 3rd edition. https://doi.org/10.1017/CBO9780511735349.
Jordan, T.E., 1981. Thrust loads and foreland basin evolution, Cretaceous, western United States. AAPG Bull. 65 (12), 2506–2520. https://doi.org/10.1306/03B599F4-16D1-11D7-8645000102C1865D.
Kumar, K.R., Honorio, H., Chandra, D., Lesueur, M., Hajibeygi, H., 2023. Comprehensive review of geomechanics of underground hydrogen storage in depleted reservoirs and salt caverns. J. Energy Storage 73, 108912. https://doi.org/10.1016/j.est.2023.108912.
Lai, J., Su, Y., Xiao, L., Zhao, F., Bai, T., Li, Y., Li, H., Huang, Y., Wang, G., Qin, Z., 2024. Application of geophysical well logs in solving geologic issues: past, present and future prospect. Geosci. Front. 15 (3), 101779. https://doi.org/10.1016/j.gsf.2024.101779.
Lalami, H.R.K., Hajialibeigi, H., Sherkati, S., Adabi, M.H., 2020. Tectonic evolution of the Zagros foreland basin since Early Cretaceous, SW Iran: Regional tectonic implications from subsidence analysis. J. Asian Earth Sci. 204, 104550. https://doi.org/10.1016/j.jseaes.2020.104550.
Mehrabi, H., Karami, F., Fakhar-Shahreza, N., Honarmand, J., 2023. Pore-type characterization and reservoir zonation of the sarvak formation in the Abadan Plain, Zagros Basin, Iran. Minerals 13 (12), 1464. https://doi.org/10.3390/min13121464.
Moos, D., Zoback, M.D., 1990. Utilization of observations of well bore failure to constrain the orientation and magnitude of crustal stresses: Application to continental, deep sea drilling project, and ocean drilling program boreholes. J. Geophys. Res. Solid Earth 95 (B6), 9305–9325. https://doi.org/10.1029/jb095ib06p09305.
Mukherjee, S., 2021. Atlas of Structural Geology. Elsevier.
Mukherjee, S., Dasgupta, S., Alsop, G.I., 2025. Structural geology in active tectonic regions: An introduction. J. Struct. Geol. 198, 10544. https://doi.org/10.1016/j.jsg.2025.105443.
Radwan, A., Sen, S., 2021. Stress path analysis for characterization of in situ stress state and effect of reservoir depletion on present-day stress magnitudes: Reservoir geomechanical modeling in the Gulf of Suez Rift Basin, Egypt. Nat. Resour. Res. 30 (1), 463–478. https://doi.org/10.1007/s11053-020-09731-2.
Rajabi, M., Sherkati, S., Bohloli, B., Tingay, M., 2010. Subsurface fracture analysis and determination of in-situ stress direction using FMI logs: An example from the Santonian carbonates (Ilam formation) in the Abadan Plain, Iran. Tectonophysics 492 (1–4), 192–200. https://doi.org/10.1016/j.tecto.2010.06.014.
Rajabi, M., Ziegler, M., Ranjbarkarami, R., Tavoosiiraj, P., 2024. A novel approach for geomechanical modelling in the absence of stress magnitude data. Austral. Energy Prod. J. 64 (2), S275–S279. https://doi.org/10.1071/ep23123.
Reisabadi, M.Z., Rajabi, M., Velayati, A., Pourmazaheri, Y., Haghighi, M., 2018. 1D mechanical earth model in a carbonate reservoir of the abadan plain, southwestern Iran: Implications for wellbore stability. In: AAPG Asia Pacific Region GTW, Pore Pressure & Geomechanics: from Exploration to Abandonment. https://doi.org/10.1306/42298Reisabadi2018.
Saadatnia, N., Sharghi, Y., Moghadasi, J., Ezati, M., 2022. Geomechanical modelling and cap-rock integrity of one of the southwest Iranian giant carbonate oil field. J. Petrol. Geomech. 5 (3), 43–60. https://doi.org/10.22107/jpg.2022.354445.1176.
Saadatnia, N., Sharghi, Y., Moghadasi, J., Ezati, M., 2024. Coupled hydro-mechanical simulation in the carbonate reservoir of a giant oil field in southwest Iran. J. Pet. Explor. Prod. Technol. 14 (1), 59–83. https://doi.org/10.1007/s13202-023-01695-2.
Sattarzadeh, Y., Cosgrove, J.W., Vita-Finzi, C., 2002. The geometry of structures in the Zagros cover rocks and its neotectonic implications. Geol. Soc. London 195 (1), 205–217. https://doi.org/10.1144/gsl.sp.2002.195.01.11.
Shamszadeh, A., Sarkarinejad, K., Ferrer, O., Mukherjee, S., Seraj, M., 2022. Interaction of inherited structures and contractional deformation in the South dezful embayment: insights from the Gachsaran oilfield, SW Iran. Mar. Petrol. Geol. 145, 105871. https://doi.org/10.1016/j.marpetgeo.2022.105871.
Stewart, S.A., 2018. Hormuz salt distribution and influence on structural style in Northeast Saudi Arabia. In: 80th EAGE Conference and Exhibition 2018. European Association of Geoscientists & Engineers. https://doi.org/10.1144/petgeo2017-011.
Sundli, K.C., Pradhan, S.P., Vishal, V., Harilal, Bhardwaj, A., Ram, B., Prasad, S.R., 2024. Stress assessment of unconventional basement reservoir in a hydrocarbon field of Western offshore India: Reservoir geomechanical modeling and perspectives. J. Geol. Soc. India 100 (11), 1568–1576. https://doi.org/10.17491/jgsi/2024/174016.
Taghipour, M., Ghafoori, M., Lashkaripour, G.R., Hafezi Moghaddas, N., Molaghab, A., 2019. Estimation of the current stress field and fault reactivation analysis in the Asmari reservoir, SW Iran. Pet. Sci. 16, 513–526. https://doi.org/10.1007/s12182-019-0331-9.
Tavoosi Iraj, P., Rajabi, M., Ranjbar-Karami, R., 2023. Integrated petrophysical and heterogeneity assessment of the Karstified Fahliyan formation in the Abadan plain, Iran. Nat. Res. Res. 32 (3), 1067–1092. https://doi.org/10.1007/s11053-023-10175-7.
Yaghoubi, A., Mahbaz, S., Dusseault, M.B., Leonenko, Y., 2021. Seismicity and the state of stress in the Dezful embayment, Zagros fold and thrust belt. Geosciences 11 (6), 254. https://doi.org/10.3390/geosciences11060254.
Yanchun, L.I., Deli, J.I.A., Suling, W.A.N.G., Ruyi, Q.U., Meixia, Q.I.A.O., He, L.I.U., 2024. Surrogate model for reservoir performance prediction with time-varying well control based on depth generative network. Petrol. Explor. Dev. 51 (5), 1287–1300. https://doi.org/10.1016/s1876-3804(25)60541-6.
Zhang, L., Yuan, X., Luo, L., Tian, Y., Zeng, S., 2023. Seepage characteristics of broken carbonaceous shale under cyclic loading and unloading conditions. Energy Fuel. 38 (2), 1192–1203. https://doi.org/10.1021/acs.energyfuels.3c04160.
Zhang, Y., Yin, S., Zhang, J., 2021. In situ stress prediction in subsurface rocks: An overview and a new method. Geofluids 2021 (1), 6639793. https://doi.org/10.1155/2021/6639793.
Zhou, H., Liu, Z., Liu, F., Shao, J., Li, G., 2024. Anisotropic strength, deformation and failure of gneiss granite under high stress and temperature coupled true triaxial compression. J. Rock Mech. Geotech. Eng. 16 (3), 860–876. https://doi.org/10.1016/j.jrmge.2023.06.012.
Zhou, H., Liu, Z., Shen, W., Feng, T., Zhang, G., 2022. Mechanical property and thermal degradation mechanism of granite in thermal-mechanical coupled triaxial compression. Int. J. Rock Mech. Min. Sci. 160, 105270. https://doi.org/10.1016/j.ijrmms.2022.105270.
Zoback, M.D., 2010. Reservoir Geomechanics. Cambridge university press.
Zoback, M.D., Mastin, L., Barton, C., 1986. In-situ stress measurements in deep boreholes using hydraulic fracturing, wellbore breakouts, and stonely wave polarization. In: ISRM International Symposium.